Publications of the Astronomical Society of the Pacific, **115**:990–1001, 2003 August
© 2003. The Astronomical Society of the Pacific. All rights reserved. Printed in U.S.A.

Photon Noise–limited Doppler Asteroseismology with a Fourier Transform Seismometer. I. Fundamental Performances

Benoît Mosser[1]

LESIA, Observatoire de Paris, F-92195 Meudon, France; benoit.mosser@obspm.fr

Jean-Pierre Maillard

Institute d'Astrophysique de Paris, 98 bis boulevard Arago, F-75014 Paris, France; maillard@iap.fr

and

François Bouchy

Observatoire de Genève, 51. ch des Maillettes, 1290 Sauverny, Switzerland; francois.bouchy@obs.unige.ch

Received 2003 January 24; accepted 2003 May 12; published 2003 June 27

ABSTRACT. The photon noise–limited performances of a Fourier transform (FT) seismometer for ground-based asteroseismological observations are computed. Simulations are conducted for a set of stars close to solar type, with V magnitude equal to 4 and $v \sin i$ from 0 to 40 km s^{-1}, extended to 100 km s^{-1} and 8500 K in order to include δ Scuti stars. Two instrumental configurations are considered and compared: the simplest one matched to a narrowband, visible spectral range, and another one that implies a low-resolution postdisperser, which covers a large portion of the visible domain. The final results are presented as the ratio of the expected uncertainties of the FT seismometer, in the version with a postdisperser, to the minimum radial velocities obtained with a grating spectrometer, on the same stellar targets. This ratio varies roughly between 1 and 2; it is close to 1 for fast rotators. It is concluded that the FT seismometer can be a challenging solution for a network dedicated to asteroseismology.

1. INTRODUCTION

The development of numerous space projects dedicated to asteroseismology shows the importance of observing and measuring seismic parameters in order to study stellar structure, stellar interior, and stellar activity. Very credible ground-based results have been recently obtained by different groups for a few bright stars. Results obtained on Procyon exhibited a large splitting of 53 ± 3 μHz and predicted a maximum amplitude of about 1 m s^{-1} for the p-modes (Mosser et al. 1998), in complete agreement with later and more precise measurements obtained by Martic et al. (1999). Bedding et al. (2001) and Carrier et al. (2001) found evidence for solar-like oscillations in β Hyd. Bouchy & Carrier (2001, 2002) presented clear evidence for the identification of the low-degree pressure mode oscillation pattern of α Cen. These results really open the field of observational asteroseismology. After single-site observations on very bright stars, network observations on various targets are necessary to fully develop the potential diagnosis of asteroseismology for studying the structure of stellar interiors.

In the continuation of seismic observations of stars and planets conducted with a Fourier transform spectrometer (FTS; Mosser et al. 1993, 1998; Mosser, Maillard, & Mékarnia 2000; Maillard 1996), we propose the examination of the fundamental capabilities of such a device for asteroseismology, to determine whether a dedicated instrument based on an interferometer can be an attractive alternative to a high-resolution echelle spectrograph designed for the same purpose. We plan to show that such a dedicated instrument can fulfill the required specifications, as it is simpler and smaller than a high-resolution echelle spectrograph for radial velocity measurements such as, for example, the High Accuracy Radial Velocity Planet Searcher (HARPS; Pepe et al. 2000).

For this analysis, photon noise is the only source of error that is considered, as was done for a grating spectrograph by Bouchy, Pepe, & Queloz (2001). This simulation will characterize the performances that can be expected to help define the required spectral coverage and make some instrumental choice to achieve the best signal-to-noise ratio (S/N). The practical design of a dedicated interferometric seismometer, which could reach photon noise–limited conditions, will be the matter of a complementary paper (Paper II: Instrumental Solution).

In the following, we first justify the need for instrumentation for ground-based observations and define the required specifications. Section 3 begins with a brief reminder of the principle of Doppler-shift measurements from an FTS. The quality factor

[1] Research associate at IAP, CNRS.

TABLE 1
SCIENTIFIC SPECIFICATIONS

Objectives	m_V	Number of Targets	Sensitivity[a]
p-modes of solar type stars (F, G, K; IV or V class)	<5	>50	G type: 10 cm s^{-1}, F type: 1 m s^{-1}
δ Scuti, rapid rotator (A stars), low-metallicity subdwarf	<8	>50	5 m s^{-1}

[a] After five nights, and 50% duty cycle, for a 4 σ detection.

of such measurements is then defined and adapted to the technique of FTSs under photon noise–limited conditions. The results of the simulation for various stellar types close to solar as a function of $v \sin i$, a stellar parameter that affects the quality factor, are described in § 4. How this technique can compare with an echelle spectrometer is presented in § 5, since so far this type of instrument has provided the best seismometric results. Finally, we conclude that even though it does not perform as well, an FT seismometer offers an attractive alternative to the classical grating spectrometer.

2. A DEDICATED INSTRUMENTATION FOR ASTEROSEISMOLOGY

2.1. Earth-based versus Space Observations

The space mission *COROT* (Baglin et al. 2002) will continuously study during 5 months five different fields with one main seismic targets plus nine secondary targets per field, and spend 1 month on a wider range of objects. The microsatellite *MOST* (Matthews, Kuschnig, & Shkolnik 2000) will follow similar aims but with more limited ambitions. These missions will essentially provide very clear and precise seismic information with a quality unachievable from Earth. However, the number of possible targets appears to be restricted, limited by strong specifications on the magnitude (bright magnitudes for the micromission *MOST*) and on the coordinates (only limited areas on the sky provide an acceptable duty cycle).

Compared to space missions, ground-based observations cannot offer continuous data acquisition on a source without the completion of a worldwide network of instruments, but they are more versatile. If the observation of a given object will not exceed 1.5 months, with a limited number of telescopes included in the network, it is possible to observe it again 1 yr later, hence obtaining very long term information that will not be provided by space observations. Ground-based observations can give access to a larger number of stellar targets, representative of the portion of the HR diagram where solar-like oscillations are expected (see Table 1; the number of targets was estimated after analysis of the bright star stellar catalogs; C. Barban 2002, private communication). Moreover, complementary observations will be possible, since space projects search for the photometric signature of the oscillation, whereas ground-based observations provide the Doppler signature. Helioseismology has shown the potential of comparing both signatures (Toutain et al. 1997).

2.2. Specifications for a Ground-based Seismometer

To be competitive with space programs, ground-based observations must be able to observe at least 50 dwarf or subgiant stars around solar type, i.e., between F and early K types. Since such observations can only be spectroscopic, slow rotators, which exhibiting narrow lines, are better candidates. The influence of the $v \sin i$ parameter on the performances will be studied in detail in this paper. The instrument has to satisfy a high stability and a high throughput to reach a sensitivity better than 10 cm s^{-1} after typically five nights, behind a 2 m class telescope. A duration of 5 days corresponds to the average lifetime of the acoustic modes. Telescopes of 2 m are currently the largest telescopes available for long-term programs and suitable to be part of a network. For the following simulations, we consider a duty cycle of only 50% as a conservative value to take into account that ground-based observations are subject to weather conditions. From a search for potential candidates, we conclude that these constraints imply that the combination of telescope plus instrument should be sensitive up to a V magnitude of 5 at least. The scientific specifications of a ground-based stellar seismometer are summarized in Table 1. δ Scuti–type stars, which represent a particular case of stellar oscillations with fewer spectral lines involved but a large amplitude, are also included. They can represent a secondary objective to consider.

3. THE FOURIER TRANSFORM SEISMOMETER

3.1. Seismometry in the Fourier Space

The principle and the application of the measurement of a Doppler signal from a small portion of an interferogram obtained with an FTS were first presented in Mosser et al. (1993). The method and further results were detailed in Maillard (1996). Later, the same principle used in a new data acquisition mode on Procyon and Jupiter was explored in Mosser et al. (1998, 2000). These papers have to be consulted for a complete description of the method with the related equations. Here, only a brief reminder is given as required to follow the development of the current paper.

In standard FT spectroscopy, the output signal of a Michelson interferometer, illuminated by a white source (a laboratory or a natural source) whose spectral domain is limited by a filter (Fig. 1*a*), is recorded as a function of the optical path difference (OPD) δ. This function $I(\delta)$ is made of the sum of the sine

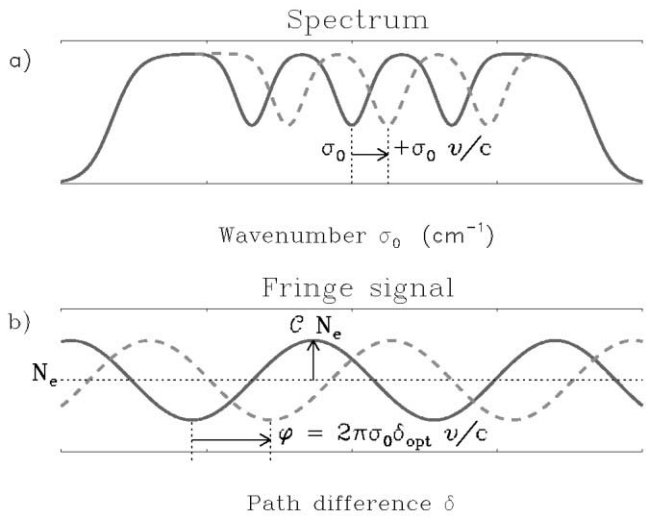

FIG. 1.—(*a*) Doppler shift in the spectrum; (*b*) Doppler shift in the interferogram, related to the phase change of the fringe of contrast C superposed on the contribution of the total flux (N_e photoelectrons).

waves corresponding to all the frequencies within the bandpass; we make the Fourier transform of $I(\delta)$ to retrieve the spectrum of the source. Around a given OPD δ_0, the signal appears as a sine wave (Fig. 1*b*) that we call a *fringe signal*, with a period equal to the mean wavelength λ_0 of the filter bandpass. If for another recording all the lines that contribute to the fringe signal are slightly shifted by a Doppler velocity v, the fringe signal appears shifted with respect to δ_0 (Fig. 1*b*). This displacement at δ_0 can be approximated as a phase shift φ of the fringe signal. It contains the Doppler velocity v, with

$$\varphi = 2\pi\sigma_0\delta_0\frac{v}{c}, \tag{1}$$

in which $\sigma_0 = 1/\lambda_0$. Thus, without recording the spectrum of the source, the Doppler signal corresponding to the displacement of all the lines as a result of the stellar pulsations can be retrieved from a temporal series of φ measurement (Mosser et al. 1998, 2000). That is the basic principle of seismometry in the Fourier space. By analogy, an FTS used this way can be called a *Fourier transform seismometer*. In the papers cited above, the high-resolution FTS at the Canada-France-Hawaii Telescope was tested in this mode.

Equation (1) shows the role of the OPD. In principle, the largest OPD value will give the largest φ value. However, to be able to determine φ supposes that the amplitude of the fringe signal is strong enough. It can be shown that for a single line, the efficiency varies like the product $\delta\Gamma(\delta)$, where $\Gamma(\delta)$ is the fringe visibility function of the line, i.e., the Fourier transform of the line profile (Maillard 1996). The function $\Gamma(\delta)$ is maximum at $\delta = 0$ and decreases with δ. Thus, there is an optimum value of $\delta = \delta_{\rm opt}$ for which the sensitivity is maximum. Figure 2, which is reproduced from Mosser et al. (2000) on real data with the CFHT-FTS, shows in practice the various steps for the determination of $\delta_{\rm opt}$. In the case of multiple lines as in these data, the function $\Gamma(\delta)$ is experimentally provided by the envelope of the interferogram $I(\delta)$.

3.2. Quality Factor

The fringe signal at $\delta_{\rm opt}$ is characterized by a contrast $C = A(\delta_{\rm opt})/N_e$, where A is the fringe intensity and N_e is the total intensity, in number of detected photoelectrons. Note that this flux corresponds to the total flux from the source within the bandpass only with a dual output FTS; otherwise, it is half of the total flux. The rms phase noise is calculated in the Appendix; its value is

$$\langle\delta\varphi\rangle = \frac{\sqrt{2}}{C\sqrt{N_e}}. \tag{2}$$

Hence, the rms velocity noise is expressed as

$$\langle\delta v_{\rm rms}\rangle = \frac{c}{2\pi\sigma_0\delta_{\rm opt}}\frac{\sqrt{2}}{C\sqrt{N_e}} = \frac{c}{Q_\lambda\sqrt{N_e}}. \tag{3}$$

The factor Q_λ, which is the quality factor of the spectrum for the Fourier transform seismometer, is expressed as

$$Q_\lambda = \sqrt{2}\pi\sigma_0\delta_{\rm opt}C. \tag{4}$$

This concept is equivalent to the quality factor introduced by Connes (1985) and used by Bouchy et al. (2001) to characterize the photon noise–limited performances for radial velocity measurements with a grating spectrometer.

The resolution of the spectrometer does not appear explicitly in equation (4), as for a grating spectrometer. However, the term $\delta_{\rm opt}$ takes its place, as it is known that for an FTS the resolution is proportional to $1/\delta$. For seismological applications, the path difference to reach depends directly on the line width Δv (in velocity) of the stellar lines. For a Lorentzian profile, the computation of $\delta_{\rm opt}$ gives (Maillard 1996)

$$\sigma_0\delta_{\rm opt} \simeq 0.32\frac{c}{\Delta v}, \tag{5}$$

which leads to the expression of the quality factor as

$$Q_\lambda \simeq 1.41\frac{c}{\Delta v}C. \tag{6}$$

According to equation (6), the best quality factor is, as expected, obtained for slow rotators (low value of Δv) and high fringe contrast C at the optimum OPD $\delta_{\rm opt}$. A high fringe contrast outside of zero path difference is provided by a strong modulation of the interferogram and depends on the density and the depth of the spectral lines in the spectrum.

The qualitative comparison of the different stellar targets

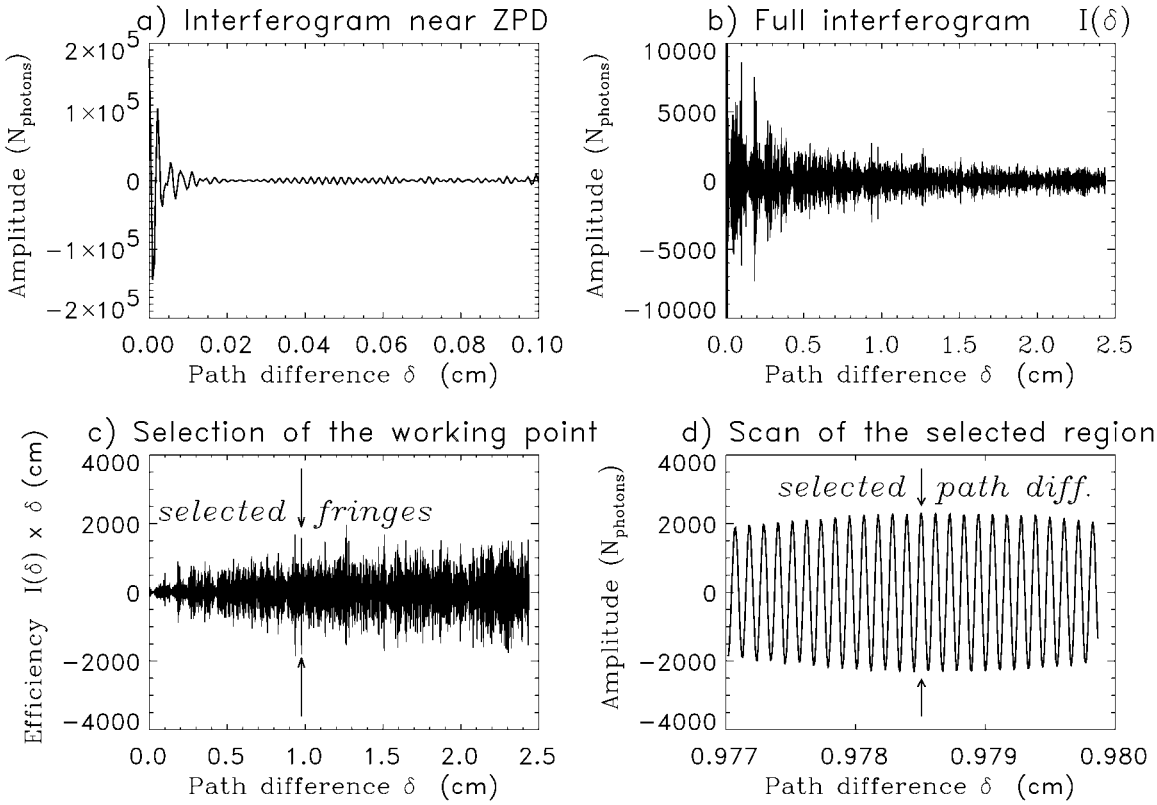

FIG. 2.—Determination of the optimum OPD for the seismological application of an FTS (adapted from Mosser et al. 2000). (*a*) Interferogram of Jupiter, near zero path difference, for a filter centered at 1100 nm (FWHM 240 nm). Intensity is scaled to the total number of photons collected through the filter; only the modulated part is represented, which explains the zero mean value. (*b*) Full interferogram $I(\delta)$, without the very first samples, to show more clearly the fringe visibility. Beyond $\delta \simeq 2$ cm, the interferogram is dominated by photon noise. (*c*) Efficiency function $\delta I(\delta)$; the highest peak out of the noise corresponds to the best working point. (*d*) Fine scanning of the fringe peak and determination of the working OPD $\delta_{\rm opt}$ at the fringe of maximum amplitude.

becomes possible with this parameter. A high value for Q_λ is produced by a rich stellar spectrum and a slow rotation rate. The quality factor will decrease with increasing line widths as a result of stellar temperature or rapid rotation. Such results are in agreement with the study of Bouchy et al. (2001) in the case of the grating spectrometer. However, an important difference must be emphasized. Let us recall the expression of the quality factor of the grating seismometer, for the bandpass $\Delta\lambda$, with the incident number of photons per spectral range $N' = dN/d\lambda$:

$$Q_{\rm GS} = \frac{\int_{\Delta\lambda} N'[(d\ln N')/(d\ln\lambda)]^2\, d\lambda}{\int_{\Delta\lambda} N'\, d\lambda}. \qquad (7)$$

This expression is concerned only with intrinsic properties of the spectrum. Introducing more spectral lines while increasing the spectral bandpass improves the performances.

The expression of the quality factor of the source in the case of the FT seismometer (eq. [4]) shows that the integration over the bandpass is expressed by the fringe contrast. In other words, the fringe contrast results from the different interference contributions. This means that the quality factors of the FT seismometer are determined not only by the intrinsic property of the stellar spectra but also by the resulting interferences over the instrumental bandpass. As a consequence, increasing the bandwidth, in most cases, will decrease the contrast, either by unconstructively co-adding the interferometric signals or by adding a useless continuum signal from regions with no spectral lines. On the other hand, the velocity noise is improved by increasing N_e (eq. [3]). Finally, both effects—integrated photoelectrons and resulting contrast—have contradictory consequences. The optimization of the principle of Doppler measurements from an FT seismometer results from their balance, which is rigorously studied by the simulations presented in the next section.

4. SIMULATION

4.1. Method

The set of synthetic spectra used in the current simulation, generated from Kurucz's database (Kurucz 1995), is the same one used by Bouchy et al. (2001) for their study of the fundamental performances of an echelle spectrometer for asteroseismology. The spectra cover the range 380–680 nm

(14,700–26,300 cm^{-1}), with an initial sampling of 5×10^{-4} nm. We consider spectral types of dwarfs with solar abundances and effective temperatures between 5000 and 7000 K. Such targets should present noticeable oscillation amplitudes (Houdek et al. 1999).

Following Bouchy et al. (2001) and Tycner & Lester (2002), we focused our attention on the visible part of the stellar spectrum. Previous observations (Mosser et al. 1998, 2000) were conducted in the near-infrared after a selection of the best domain, only because the CFHT-FTS detectors were matched to the 1–5 μm range. Equation (6) justifies the choice of the visible, since Q_λ is directly proportional to the fringe contrast C. High contrasts are associated to spectral ranges with numerous deep lines. Such lines are mostly encountered in the bluer part of the spectrum of solar-type stars.

Each visible spectrum was divided into small spectral ranges, with both adjustable central wavelength and bandwidth. For each bandwidth, we calculated a synthetic interferogram, from which we derived the best path difference δ_{opt} as well as the associated contrast C. The bandwidth profile creates a strong modulation near zero OPD. By an estimation of the minimum OPD from which to start the path difference exploration, numerical simulations allowed us to take care that the contrast was effectively due to the spectral lines and not to the selected bandwidth profile. Then, according to equation (4), we derive the quality factor Q_λ.

In order to quantify the rms performance $\langle \delta v_{rms} \rangle$, the sensitivity was calculated under the following assumptions: a network of 2 m class telescopes, providing a duty cycle of 50%, and a 4 mag star. The only source of noise considered in the simulation is photon noise. Realistic data were taken for the parameters of the simulations: atmospheric transmission at zenith but at sea level, optical efficiency of the telescope and of the instrument based on the schematic layout of the CFHT-FTS, and quantum efficiency of the CCD detector. The overall efficiency $\tau(\lambda)$ of the instrument, namely, the ratio of detected photoelectrons/stellar photons, was introduced in a reformulation of equation (3):

$$\langle \delta v_{rms} \rangle = \frac{c}{Q_\lambda \sqrt{\tau(\lambda)\Delta\lambda N'}}, \tag{8}$$

where $\Delta\lambda$ is the spectral range and $N' = dN/\Delta\lambda$ is the incident number of photons per spectral range. The function $\tau(\lambda)$ is shown in Figure 3 for the two instrumental configurations described below.

4.2. Single Bandpass (FS1)

Photon noise–limited performances were computed in the case of a single bandpass defined by a portion of stellar spectrum of bandwidth $\Delta\lambda$, according to equations (8) and (4) for the FT seismometer or equation (7) for the grating spectrometer, in each case with the relevant $\tau(\lambda)$ function. Actually, such a simulation represents the mode of observation conducted with the CFHT-FTS, where a narrowband filter selecting a small region with deep lines was placed in front of the detectors. For each spectrum, the best fundamental performance was searched for, and the parameters of the best solutions were analyzed: location and width of the bandpass, δ_{opt} from 1 cm when the rotational velocity $v \sin i = 0$ km s^{-1}, down to 0.2 cm when $v \sin i = 20$ km s^{-1}, and bandpass varying from 0.3 to 4 nm.

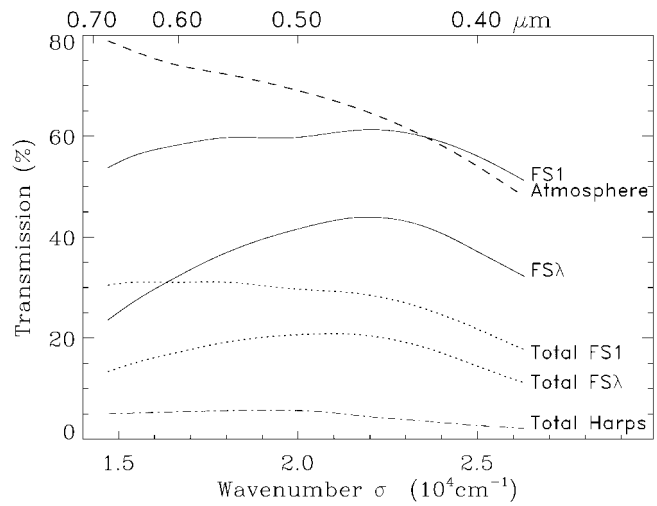

FIG. 3.—Transmission curves introduced in the simulation. The atmospheric transmission is taken at zenith, but sea level. The total optical efficiency $\tau(\lambda)$ of the FT seismometer (FS1: single bandpass; FSλ: multibandpass; see § 4.3) includes all optical parts, in reference to the CFHT-FTS, plus the quantum efficiency of the CCD. The efficiency of the HARPS spectrograph (Pepe et al. 2000) is also shown.

Figure 4 presents the variation of Q_λ with the bandpass $\Delta\lambda$ for different regions of the visible spectrum; Q_λ decreases with $\Delta\lambda$ as $(\Delta\lambda)^{1/2}$. It is not possible to obtain, at the same time, a high value for the quality factor Q_λ and a wide bandpass $\Delta\lambda$, since increasing $\Delta\lambda$ drastically reduces the contrast of the fringe. However, the wide scattering of Q_λ for a given bandwidth is indicative of the large variation of the line density along a spectrum, which induces large variation of the fringe contrast C.

When testing the different stellar types at different rotational velocity, it appears that both best bandpass and best path difference vary in very broad domains, which is not favorable for the definition of an instrument that we hope to be as simple as possible. Furthermore, the best bandpass, around a few nanometers or less, is so narrow that it should require a Fabry-Perot filter, which implies strong instrumental constraints to achieve the necessary stability. Finally, the best results obtained with a single bandpass are not competitive with the photon noise–limited results provided by a grating spectrometer, since the best rms velocity limit is more than 6 times larger. This is mainly because the photoelectron number is quite reduced by

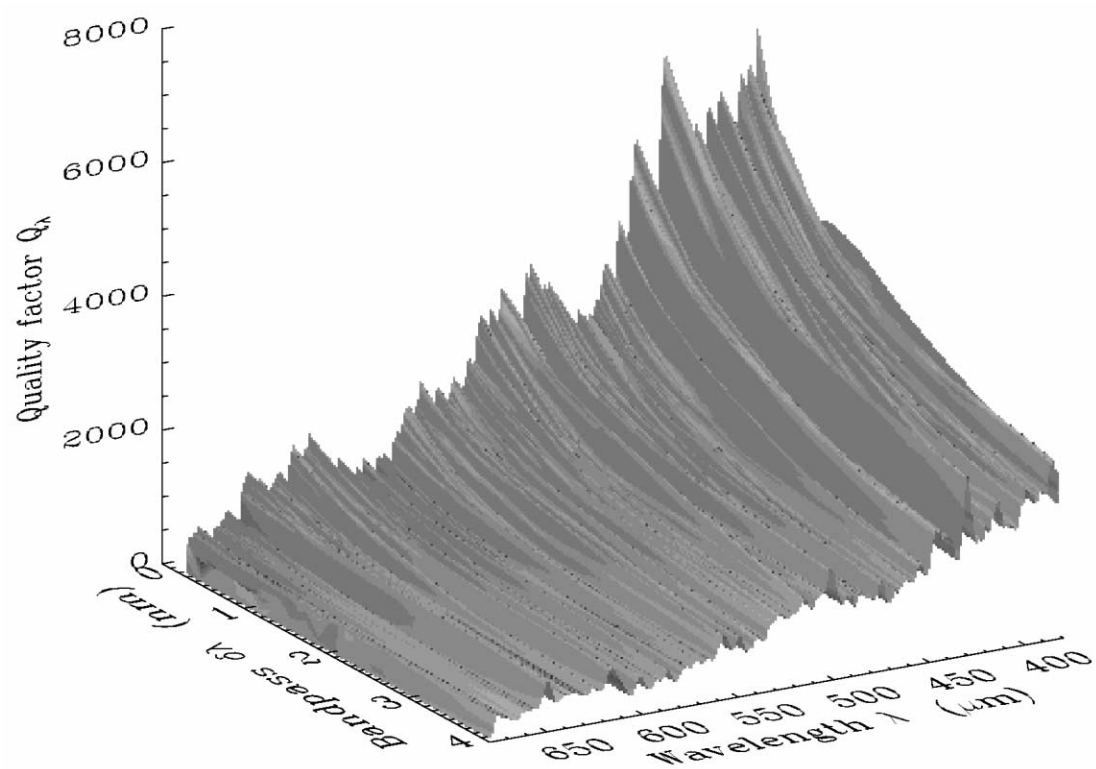

FIG. 4.—Quality factor as a function of the filter bandwidth and of the wavelength for the single-bandpass configuration (FS1) for an F9 V star with $v \sin i = 0$ km s^{-1}. The high Q_λ values are clearly due to the blue part of the spectrum, whereas the red part contributes only to low values.

a limited spectral range. Table 2 presents the ratio of the photon noise–limited velocity $\delta v_{\rm FS1}/\delta v_{\rm GS}$ obtained with a single bandpass (FS1) compared to a grating spectrometer (GS).

It appears necessary to extend the number of detectable photoelectrons but without reducing the fringe contrast. The solution must be the simultaneous access to many adjacent narrowband filters. This can be obtained by the simple addition to the interferometer of a low-resolution postdispersion system.

4.3. Multiple Bandpass (FSλ)

The conclusion of the previous section is equivalent to the discussion on the multiplex advantage of an FTS with respect to the spectral bandpass. In photon noise conditions, increasing the bandpass of a spectrum obtained with an FTS decreases the S/N coarsely as $\sqrt{\mathcal{N}}$, where $\mathcal{N}$ is the number of spectral elements, since the photon noise from the full bandpass is received on the single detector (or two with a dual-output FTS). With a postdispersion system behind the FTS, a small spectrum is imaged on an array detector.

TABLE 2
SPEED UNCERTAINTIES IN SINGLE-BANDPASS MODE

Spectral Type	$v \sin i$ (km s^{-1}) 0	20
K2 V ……	9.8	8.5
F9 V ……	7.2	7.5
F2 V ……	7.7	6.7

High resolution is provided by the FTS while the noise in the spectrum is reduced since the photon noise comes from only the narrow spectral range seen by 1 pixel. Such a solution avoids the $\sqrt{\mathcal{N}}$ S/N decrease. This idea was tested for the first time by Jennings et al. (1986) on a facility FTS in a region of high background emission at 10 μm. The same principle can be applied to an FT seismometer to have access to a large spectral range to increase the Doppler velocity information from the stellar spectrum without increasing the photon noise from the total flux. The low-resolution postdispersion was simulated as provided by a reflection grating with an efficient reflecting factor in a broad visible bandpass $\Delta\lambda$. The limit of resolution $\delta\lambda$ defines the possible recording of $\mathcal{N} = \Delta\lambda/\delta\lambda$ different interferograms at the same path difference over the total bandpass $\Delta\lambda$.

4.3.1. Performance

When considering the contribution of the different band-

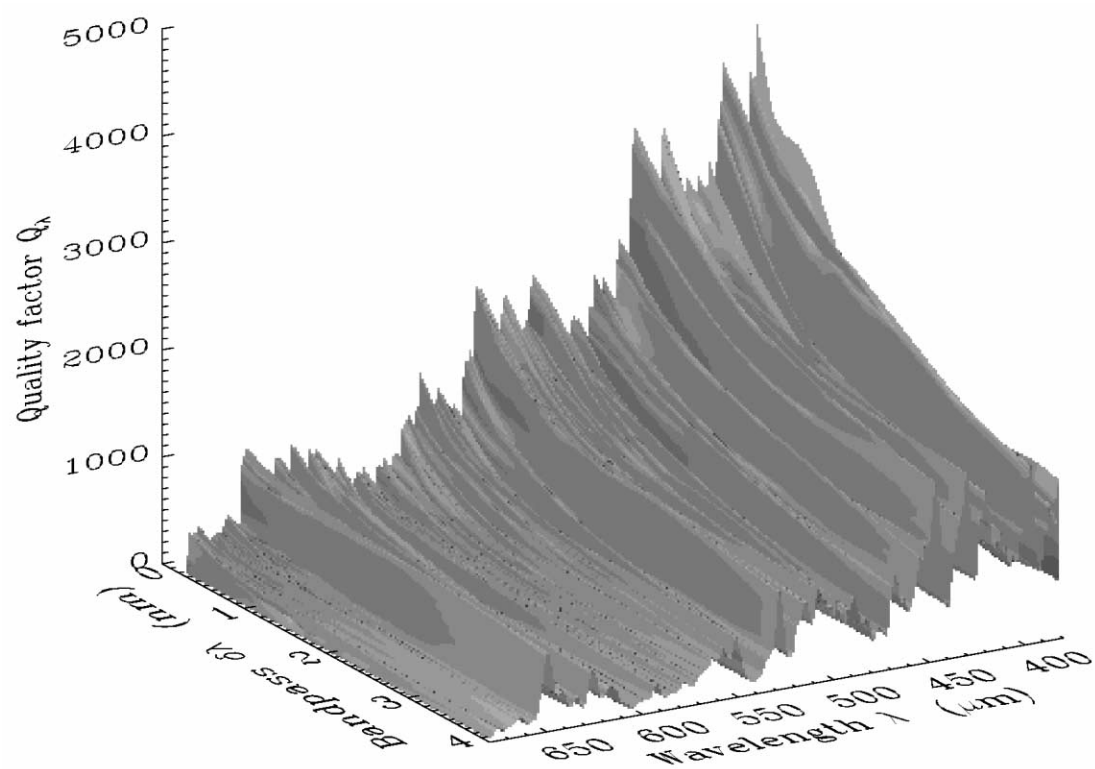

FIG. 5.—Same as Fig. 4, for the same bandwidths, but for the multibandpass configuration (FSλ). In that case, as opposed to Fig. 4, the optimum path difference has to be calculated for the whole spectrum. As a result, the Q_λ values are lower than for Fig. 4.

passes, the velocity limit results from the weighted average

$$\langle \delta v \rangle^{-2} = \sum_\lambda \langle \delta v_\lambda \rangle^{-2}. \tag{9}$$

In order to validate this equation, and according to equation (8), the integrated quality factor has to be calculated as

$$Q = \frac{\sqrt{\int_{\Delta\lambda} d(N_\lambda/d\lambda) Q_\lambda^2 \, d\lambda}}{\sqrt{\int_{\Delta\lambda} d(N_\lambda/d\lambda) \, d\lambda}}. \tag{10}$$

Compared to the single-bandpass case, the performances obtained with postdispersion are derived from the compromise between lower quality factor values (Fig. 5) but higher intensity. The decrease of the quality factors of each single bandpass results from the fact that the optimum path difference is now constant over the whole spectrum and is not optimum for each individual bandpass. As a consequence, the gain in S/N is lower than $\sqrt{N}$. However, the performances for an F2 V slowly rotating star are about 6 times better than with a single spectral range and are 11 times better for a K2 V star. For rapid rotators, the gains are, respectively, 4 and 6 for F2 V and K2 V stars.

Table 3 presents the example of an F9 V slowly rotating star ($v \sin i = 0$ km s^{-1}), for which the gain is 8. It shows the properties of the distribution of the Q values of the interferograms of the different 10 cm^{-1} broad bandpass of the stellar spectrum. The properties (numbers of ranges, contribution to the flux, integrated quality factor, rms velocity noise, and integrated rms velocity noise) have been calculated according to the range of the quality factor. The mean values of Q and $\langle \delta v \rangle$, respectively, $\overline{Q}$ and $\overline{\langle \delta v \rangle}$, are integrated from 0 to $Q_{\rm sup}$. The best contribution, related to the best compromise between Q and the total flux, is obtained for the bandpasses having a Q value between 2000 and 3000. This table also shows the

TABLE 3
QUALITY FACTOR DISTRIBUTION

Q Range ($Q_{\rm inf}$–$Q_{\rm sup}$)	Number of Ranges	Flux (%)	$\overline{Q}$	$\langle \delta v \rangle$ (cm s^{-1})	$\overline{\langle \delta v \rangle}$ (cm s^{-1})
0–1000	464	47.0	559	7.4	7.4
1000–2000	310	32.1	1018	3.5	3.1
2000–3000[a]	129	11.8	1296	3.4	2.3
3000–4000	61	4.9	1468	3.9	2.0
4000–5000	40	2.6	1612	4.1	1.8
5000–6000	16	0.9	1689	5.4	1.7
6000–7000	8	0.6	1751	5.9	1.6
7000–8000	2	0.1	1766	12.2	1.6
FS1	1	0.1	7890	13	...
FSλ	All	100	1766	...	1.6

[a] Best contribution.

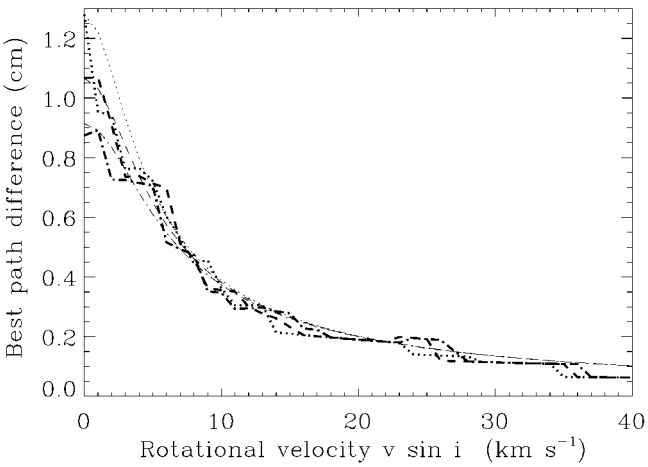

FIG. 6.—Best path difference as a function of the rotational velocity, for a K2 V (*dotted line*), F9 V (*dashed line*), or F2 V (*dash-dotted line*) star. The thin lines are the fits determined according to eq. (11). The rotational broadening becomes dominant for $v \sin i > 8$ km s^{-1}. Hence, at large rotational velocity, the best path difference does not depend on the spectral type.

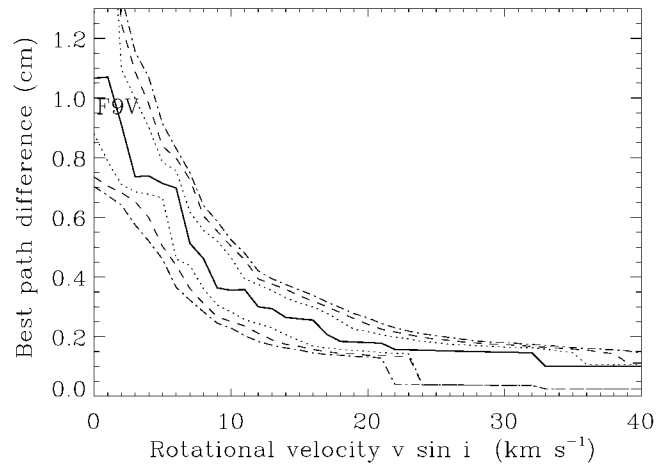

FIG. 7.—Best path difference domain as a function of the rotational velocity, for an F9 V star (*solid line*). The other lines determine the domain where the performances of the detection are reduced by less than 5% (*dotted line*), 10% (*dashed line*), and 15% (*dash-dotted line*) compared to the best path difference.

gain for an FT seismometer with a multibandpass system (FSλ) compared to a single bandpass (FS1).

4.3.2. Best Path Difference

The best path difference $\delta_{\rm opt}$ depends closely on the line width (eq. [5]), hence its intrinsic value is determined by the stellar type convolved by the stellar rotation (Fig. 6). The precise determination of $\delta_{\rm opt}$ is crucial only when a single bandpass is considered. The beating between the few lines within the bandpass defines very precise path differences. With a postdispersive system, the best path difference domain is much wider, since the possible beating between the numerous lines can occur in a large path difference range. It is important to find the range that provides performances within 10% of the best one. This domain is as large as $\pm 25\%$ around the best OPD, as shown in Figure 7. The simulation shows a clear fit of the best path difference (Fig. 6), according to the stellar temperature T_0 and to the rotational factor $v \sin i$:

$$\delta_{\rm opt}(T_0,\ v \sin i) \simeq \delta_0 \left[1 + \left(\frac{v \sin i}{v_0}\right)^2\right]^{-1/2}, \qquad (11)$$

where the fitted parameters $\delta_0 = \alpha/T_0$ and $v_0 = T_0/\beta$ ($\alpha =$ 6400 cm K and $\beta = 1560$ km^{-1} s K). This fit just respects the asymptotic variation of $\delta_{\rm opt}(T_0,\ v \sin i)$. For $v \sin i = 0$ km s^{-1}, $\delta_{\rm opt}$ varies as T_0^{-1}; at large $v \sin i$, $\delta_{\rm opt}$ varies as $(v \sin i)^{-1}$, independently of T_0.

4.3.3. Integrated Quality Factor

The variations of the integrated quality factor Q were calculated according to different parameters. As already noticed by Bouchy et al. (2001) and Tycner & Lester (2002), the blue part of the visible spectrum contributes with a much higher quality to the seismic signature because of the higher density of deep lines. The mean contrast in quality varies from 1 (15,000 cm^{-1}, 666 nm) to 5 (25,000 cm^{-1}, 400 nm). This behavior will have, of course, a strong implication on the spectral range to be observed for asteroseismology.

The rotational broadening lowers the quality factor (Fig. 8). As noticed by Bouchy et al. (2001), the influence of the

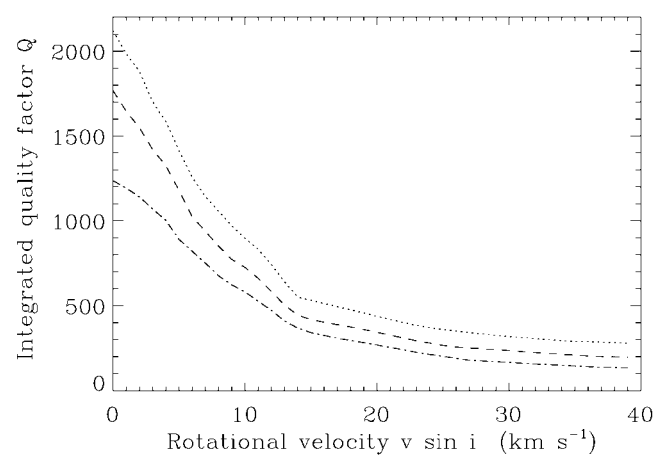

FIG. 8.—Integrated quality factor as a function of the rotational velocity $v \sin i$, for a K2 V (*dotted line*), F9 V (*dashed line*), or F2 V (*dash-dotted line*) star.

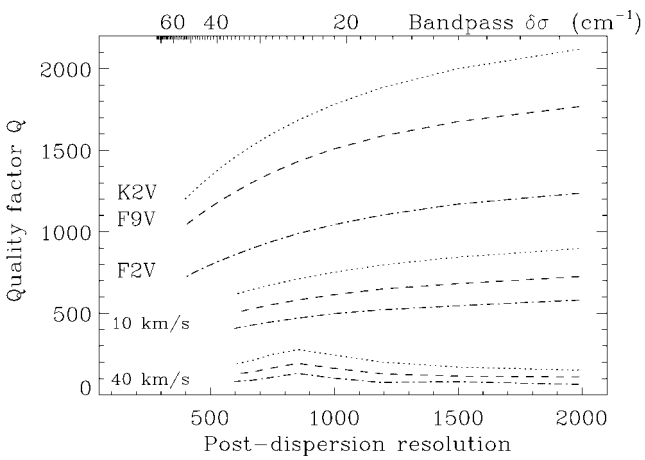

FIG. 9.—Quality factor as a function of the spectral resolution provided by the postdispersion for a K2 V (*dotted line*), F9 V (*dashed line*), or F2 V (*dash-dotted line*) star, in the case $v \sin i = 0$ (*top group*), 10 (*middle group*), or 40 km s^{-1} (*bottom group*). With broad lines, the increase of resolution does not improve the Q factor, since it becomes impossible to disentangle the fringes because of the lines from the interference pattern resulting from too narrow a bandpass.

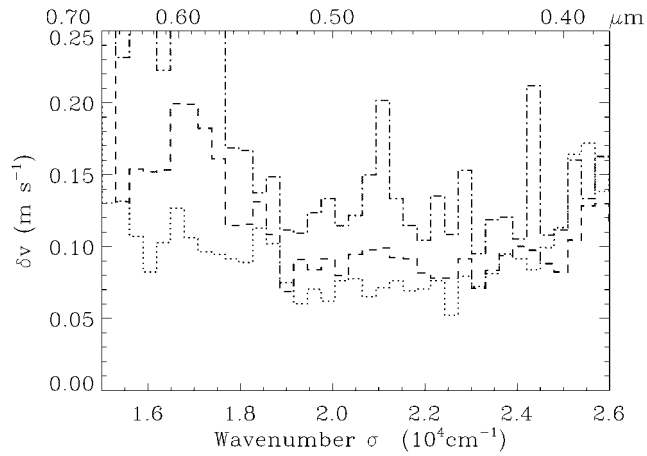

FIG. 10.—Limit of velocity due to photon noise as a function of the wavenumber for a K2 V (*dotted line*), F9 V (*dashed line*), or F2 V (*dash-dotted line*) star of 4th magnitude, with $v \sin i = 0$ km s^{-1}. Each bandpass is about 30 cm^{-1} ($\simeq$0.75 nm).

rotational broadening depends on the blending of the spectral lines. Contrary to the results reported by Bouchy et al. (2001), the decrease at high rotational velocity is less pronounced than $(v \sin i)^{-1}$. At high rotational velocity, the blending between spectral lines makes Q proportional to $(v \sin i)^{-0.7}$.

4.3.4. Postdispersion Resolution

The factor Q also depends on the spectral resolution provided by the postdispersion system (Fig. 9). For low $v \sin i$, enhancing the resolution makes it possible to achieve a better contrast in the interferogram, hence a better quality factor. For high $v \sin i$, the contrast of the fringes becomes influenced by the narrow bandwidth profiles. There is no more advantage in increasing the postdispersion resolution beyond $\simeq$800.

4.3.5. Best Bandpass

The combination of the variations of the quality factor and of the spectral energy distribution defines the bandpass contributing to most of the signal (Figs. 10 and 11). On the red side, the low performances are due to the fact that the fringe contrasts are not important for wavenumbers lower than 18,000 cm^{-1} (560 nm). On the blue side, both photon numbers and CCD efficiency decrease significantly beyond 25,000 cm^{-1} (400 nm). Thus, the most favorable range for searching for the signal lies between 18,000 and 25,000 cm^{-1}. This 160 nm wide spectral range contributes to more than 90% of the performance (Fig. 12) and must be favored for the design of an FT seismometer.

5. DISCUSSION

The previous analysis permits then the quantitative definition of the performances of the FT seismometer, as a function of the spectral type and the rotational velocity, for a given magnitude. The results are presented in Figure 12. The domain of the parameters $v \sin i$ and T_0 was extended to 100 km s^{-1} and 8500 K in order to include pulsators as δ Scuti stars (Fig. 13). The performances are well in agreement with the specifications presented in Table 1. The numbers of possible targets make possible an asteroseismic campaign that exhaustively examines the region of the HR diagram with solar-like or δ Scuti pulsators. These performances are then compared with the ones

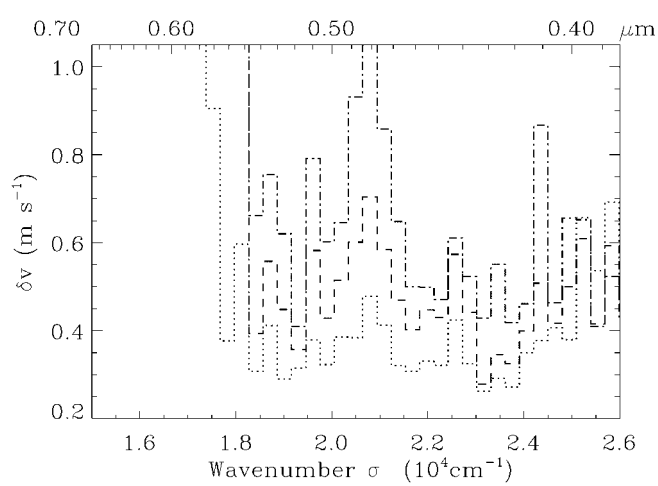

FIG. 11.—Same as Fig. 10, but with $v \sin i = 20$ km s^{-1}. The contribution of the red part of the spectrum becomes negligible.

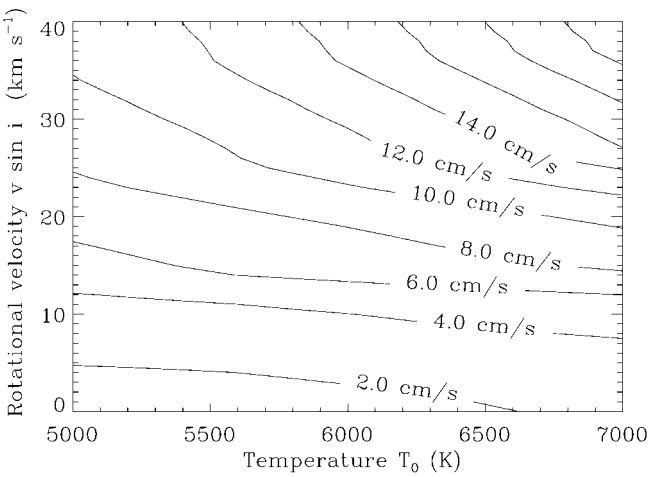

FIG. 12.—Performance $\langle \delta v_{\rm rms} \rangle$ as a function of effective temperature and $v \sin i$, obtained in the following conditions: network of 2 m class telescopes, five nights with a global duty cycle 50%, and 4th magnitude star. Such performances make it possible to fulfill the specifications of Table 1.

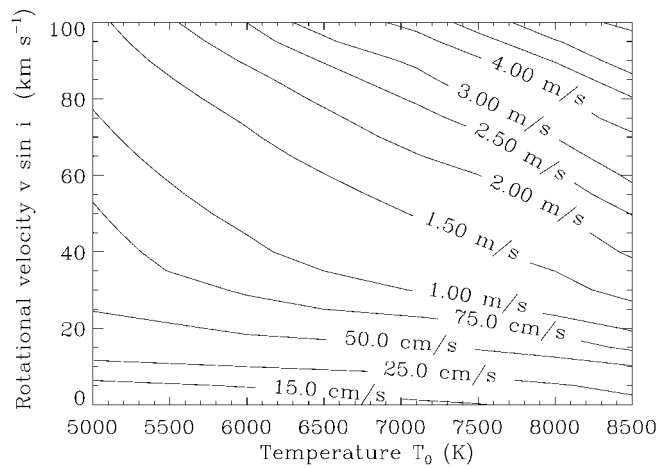

FIG. 13.—Same as Fig. 12, but for an 8th magnitude star and extended to high $v \sin i$ and T_0, to include δ Scuti–type stars.

obtained with a grating seismometer under the same conditions. Simulations were run in parallel for both methods. Thus, the comparison insures a strict equality in the treatment of the stellar spectrum and flux and is not affected by observing parameters such as the telescope size.

Figure 14 presents a direct comparison in the (T_0, $v \sin i$) space. It appears that the lower quality factors obtained with the FT seismometer are partially compensated for by higher photon counts for the FT seismometer than for the grating seismometer. The complete instrument, with a fiber alimentation and a grating for low-resolution postdispersion, presents an efficiency peaking at about 45%, so that the total efficiency, including the atmosphere and the telescope (Fig. 3), is larger than for a grating spectrometer dedicated to precise Doppler measurements, such as the HARPS instrument (Pepe et al. 2000). The minimum detectable velocity appears to be on average a factor of 1.8 greater for the FT seismometer than for the grating seismometer. If the observations are really limited by the photon noise, another way to express this comparison is that the grating seismometer can achieve comparable performance to the FT seismometer on targets 1.3 mag dimmer. It must be noticed that the FT seismometer performances are less sensitive to rotational velocity. For rapid rotators, the grating seismometer does not benefit from its high spectral resolution. On the other hand, the Doppler measurement provided by the FT seismometer is not directly related to the spectral resolution, since the information is only on the line positions, without completely resolving the line profiles.

In conclusion, for photon noise–limited performances, the most efficient instrument is without contest the grating spectrometer. However, as shown by Figure 14, the gain factor is always less than 2 with respect to the FT seismometer. In addition, for a complete comparison, one should also discuss the influence of the other potential sources of noise, such as stellar noise, seeing, scintillation, and instrumental stability. Other factors must also be considered to compare the two principles as fairly as possible, such as the overall dimensions of the instrument, data reduction, calibration, and versatility. All these points are addressed in Paper II. Already, it is obvious that with an optical path difference of about 1.2 cm at the most (Fig. 6), the FT seismometer can be a compact instrument

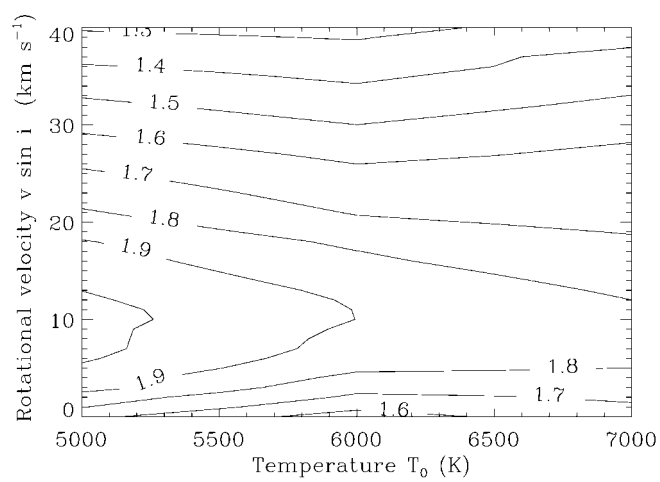

FIG. 14.—Ratio of the expected uncertainties $\delta v_{\rm FS}/\delta v_{\rm GS}$, as a function of the stellar temperature T_0 and rotational velocity, for the following spectral resolutions: 84,000 (grating seismometer) and 1200 (FT seismometer with a postdispersion system). This ratio presents local discontinuities due to particular additions of constructive interferences in the interferogram. The global trend, a smaller ratio at high rotational velocity, results from the balance of the reduced performances for both principles; the grating seismometer does not benefit from the high spectral resolution, whereas the FT seismometer does not benefit completely from the multibandpass resolution (Fig. 9).

compared to a high-resolution (≃84,000 for HARPS) echelle spectrometer. Such considerations are important for a network that supposes to have three or more instruments to duplicate.

6. CONCLUSIONS

The fundamental velocity noise, limited by the photon noise, has been calculated for a Fourier transform seismometer. The performances were calculated from synthetic stellar spectra close to solar. The principle becomes efficient and competitive as soon as the Fourier transform spectrometer is coupled to a low-resolution dispersion. Then, the optimum spectral range to conduct the observations was determined to be 18,000–25,000 cm^{-1} (400–560 nm). The best path difference was also determined and is constrained essentially by the rotational velocity.

The analysis shows the capability of Fourier seismometry to provide competitive results on a good-sized sample of solar-type dwarfs and possibly on δ Scuti stars with a network of 2 m telescopes. Even if the performances remain a factor of about 1.8 lower than for a grating spectrometer, other factors such as the dimensions and the simplicity of use (hence probably the total cost) justify consideration of it as a valid solution for a network devoted to asteroseismology. Practically, a network could be composed of both types of instruments. A precise description of such an instrument will be presented in Paper II.

This work was supported financially by the ACI (Action Concertée Incitative Jeune Chercheur of the Ministère de l'Education Nationale, de la Recherche, et de la Technologie). It benefitted from fruitful discussions with the members of the ACI (Caroline Barban, Eric Michel, and Jérôme Schmitt). We thank Claude Catala for providing us with δ Scuti models, generated from the Kurucz database (Kurucz 1995). We also thank F. Pepe and an anonymous referee for their pertinent comments.

APPENDIX

DETERMINATION OF THE PHASE OF THE FRINGE SIGNAL

The seismic observable is the varying phase φ of one fringe of the interferogram around the optimum OPD $\delta_{\rm opt}$:

$$I(\delta) = A\cos(2\pi\sigma_0\delta + \varphi) + B.$$

The amplitude A corresponds to the fringe contrast C according to $A \equiv CN_e$, whereas the term B is due to the total number of photoelectron N_e: $B \equiv N_e$, with the noise $\langle\delta B\rangle \equiv \sqrt{N_e}$. The recording of the signal over one fringe gives access to φ. With a more simple notation, $I = A\cos(x + \varphi) + B$, one calculates

$$\int_0^{2\pi} I\sin x\,dx = \frac{A}{2}\sin\varphi + \int_0^{2\pi} B\sin x\,dx, \tag{A1}$$

$$\int_0^{2\pi} I\cos x\,dx = \frac{A}{2}\cos\varphi + \int_0^{2\pi} B\cos x\,dx. \tag{A2}$$

The measured phase $\psi = \varphi + d\varphi$ is defined by

$$\tan\psi = \frac{\int I\sin x\,dx}{\int I\cos x\,dx}.$$

In practicality, ψ is determined as

$$\tan\psi = \frac{\sum_{i=1}^{p} I(\delta_i)\sin 2\pi\sigma_0\delta_i}{\sum_{i=1}^{p} I(\delta_i)\cos 2\pi\sigma_0\delta_i},$$

with p positions along the fringe. The development of $\tan\psi$ as a function of $\tan\varphi$ helps to determine the uncertainty $d\varphi$:

$$\tan d\varphi = \frac{\cos\varphi\int B\sin x\,dx - \sin\varphi\int B\cos x\,dx}{A/2 + \sin\varphi\int B\sin x\,dx + \cos\varphi\int B\cos x\,dx},$$

which gives the rms noise $\langle\delta\varphi\rangle$:

$$\langle\delta\varphi\rangle = \sqrt{(d\varphi)^2} = \frac{2}{A}\sqrt{\cos^2\varphi\langle\delta\int B\sin x\,dx\rangle^2 + \sin^2\varphi\langle\delta\int B\cos x\,dx\rangle^2}.$$

Finally, with $\langle\delta\int B\sin x\,dx\rangle = \langle\delta\int B\cos x\,dx\rangle = (N_e/2)^{1/2}$, the rms phase noise expresses as

$$\langle\delta\varphi\rangle = \frac{\sqrt{2}}{C\sqrt{N_e}}.$$

REFERENCES

Baglin, A., Auvergne, M., Catala, C., Michel, E., Goupil, M.-J., Samadi, R., & Popielsky, B. 2002, in ASP Conf. Ser. 259, Radial and Nonradial Pulsation as Probes of Stellar Physics, ed. C. Aerts, T. R Bedding, & J. Christensen-Dalsgaard (San Francisco: ASP), 626

Bedding, T. R., et al. 2001, ApJ, 549, L105

Bouchy, F., & Carrier, F. 2001, A&A, 374, L5

———. 2002, A&A, 390, 205

Bouchy, F., Pepe, F., & Queloz, D. 2001, A&A, 374, 733

Carrier, F., et al. 2001, A&A, 378, 142

Connes, P. 1985, Ap&SS, 110, 211

Houdek, G., Balmforth, N. J., Christensen-Dalsgaard, J., & Gough D. O. 1999, A&A, 351, 582

Jennings, D. E., Deming, D., Wiedemann, G. R., & Keady, J. J. 1986, ApJ, 310, L39

Kurucz R. L. 1995, in ASP Conf. Ser. 81, Laboratory and Astronomical High-Resolution Spectra, ed. A. J. Sauval, R. Blomme, & N. Grevesse (San Francisco: ASP), 583

Maillard, J. P. 1996, Appl. Opt., 35, 2734

Martic, M., et al. 1999, A&A, 351, 993

Matthews, J., Kuschnig, R., & Shkolnik, E. 2000, in Proc. SOHO 10/GONG 2000 Workshop, Helio- and Asteroseismology at the Dawn of the Millennium, ed. A. Wilson (ESA SP-464; Noordwijk: ESA), 385

Mosser, B., Maillard, J. P., & Mékarnia, D. 2000, Icarus, 144, 104

Mosser, B., Maillard, J. P., Mékarnia, D., & Gay, J. 1998, A&A, 340, 457

Mosser, B., Mékarnia, D., Maillard, J. P., Gay, J., Gautier, D., & Delache, P. 1993, A&A, 267, 604

Pepe, F., et al. 2000, Proc. SPIE, 4008, 582

Toutain, T., et al. 1997, Sol. Phys., 175, 311

Tycner, C., & Lester, J. B. 2002, PASP, 114, 330